Supplemental Material

Bulletin of the American Meteorological Society
CAIPEEX: Indian Cloud Seeding Scientific Experiment
https://doi.org/10.1175/BAMS-D-21-0291.2

Title: CAIPEEX - Indian cloud seeding scientific experiment

(Supplementary Material)

Thara Prabhakaran[1*], P. Murugavel[1], Mahen Konwar[1], Neelam Malap[1] , K. Gayatri[1], Shivsai Dixit[1], Soumya Samanta[1], Subharthi Chowdhuri[1,8], Sudarsan Bera[1], Mercy Varghese[1], J. Rao[1], J. Sandeep[1], P. D. Safai[1], A. K. Sahai[1], Duncan Axisa[5], A. Karipot[2], Darrel Baumgardner[4], Benjamin Werden[6], Ed Fortner[6], Kurt Hiebert[9], Sathy Nair[1], Shivdas Bankar[1], Dinesh Gurnule[1], Kiran Todekar[1], Jerry Jose[11], V. Jayachandran[1], Pawan S. Soyam[1], Abhishek Gupta[1], Harish Choudhary[1], Aravindhavel[1], Suresh Babu Kantipudi[1], P. Pradeepkumar[2], R. Krishnan[1], K. Nandakumar[11], Peter F. DeCarlo[10], Doug Worsnop[6], G. S. Bhat[3], M. Rajeevan[7], Ravi Nanjundiah[1,3]

1 Indian Institute of Tropical Meteorology, Ministry of Earth Sciences, Dr. Homibhabha road, Pashan, Pune, Maharashtra state, India.

2 Department of Atmospheric and Space Sciences, SPPU, Maharashtra state, India.

3 Centre for Atmospheric and Oceanic Sciences, Indian Institute of Science, Bengaluru, Karnataka state, 360 012, India.

4 Droplet Measurement Technologies, Longmont, Colorado 80503 USA.

5 Center for Western Weather and Water Extremes, SCRIPPS Institute of Oceanography, 8622 Kennel Way, La Jolla, CA 92037, USA.

6 Aerodyne Research Inc., 45 Manning Road, Billerica, MA 01821-3934, USA

7 National Centre for Earth Science Studies, Ministry of Earth Sciences, Akkulam,

Thiruvananthapuram – 695 011, India

8 Department of Civil and Environmental Engineering, University of California, Irvine, California 92697, USA

9 Weather Modification Inc., 3802 20th St. N, Fargo, ND 58102 USA

10 Johns Hopkins University, Baltimore, MD 21218, USA

11 M. G. University, Priyadarsini Hills Post, University Campus Rd, Athirampuzha, Kerala 686560, India.

*Corresponding Author Address

Thara Prabhakaran

Indian Institute of Tropical Meteorology

Dr. Homi Bhabha Road, Pashan, Pune 411008

Phone: 91 20 25904371 / 91 9422294113 (Mobile)

email: thara@tropmet.res.in

Supplement A : List of different cloud seeding experiments

Table 1 Major Research experiments in the Peer-reviewed Literature

Experiment	**Randomization** **Physical** **Numerical simulation**	**Reference**
South African Experiment over 5 Years Flares were developed and used	127 cases Radar	Mather et al. (1997):
Mexican Experiment	94 cases (43 seeded, 51 no-seed)	Bruintjes et al. (2001)
Thailand Experiment: 4 years	67 experimental units: (34 seeded and 33 nonseeded) The multiplicity of response variables rendered the p-values inconclusive	Silverman and Sukarnjanaset (2000) WMO (2000)
Indian Experiment	Though statistically significant result, there is an issue due to the merging of clouds.	Murty et al. (2000)
The UAE Research Program for Rain Enhancement Science (UAEREP) Started in 2001. Hygroscopic seeding is inconclusive, Continuing as a major research program and operational seeding.	There were 134 cases, and 96 qualified from Oman Mountains seeding. Statistical and physical evaluation	Semeniuk et al. (2014), Hosari et al. (2021)
Texas Experiment in Augmenting Rainfall through Cloud Seeding (TEXARC) program, USA (from 1996; hygroscopic physical study	Showed flares were inefficient	Rosenfeld et al. (2010)
Queensland Cloud Seeding Research Program (QCSRP), Australia. 2009: for two reasons	Resulted in 62+65 randomized cases Also led to several cloud physics studies	Tessendorf et al. (2010)
Chinese experiment for rain reduction program: in stratiform clouds.	Reduction in precipitation	Wang et al. (2019a)
Cloud Aerosol Interaction and Precipitation Enhancement Experiment (CAIPEEX), India: The present study	276 randomized cases, 151 seeded, 125 no-seed Ground-based radar, aircraft, randomization, numerical investigations	This study

Japanese Cloud Seeding Experiments for Precipitation Augmentation (JCSEPA)	Used hygroscopic flare and salt micro powder, cloud chamber experiments, hydrological modeling, airborne experiments, use of remote sensing data, etc. 'Hygroscopic seeding in the warm season may be effective in limited conditions' 2006-2011	Kuba and Murakami (2010), Yamashita et al. (2011), Koshida et al. (2012), Murakami et al. (2011), Sakai et al. (2013), Yamashita et al. (2015)
Snowy Precipitation Enhancement Research Project (SPERP), Australia	107 Experimental units targeting seeding material established	Manton et al. (2011)
Experiments on precipitation enhancement in Syria, Iran and Portugal)	Syria 1991-2000- Increase in rainfall of about 4.8-16.5 % Portugal 1999: 7.4 % increase	Dinevich et al. (2008)
Chinese Weather Modification Project (2006-2010),	Seeding in the maximum updraft region or maximum supercooled water region can obtain the largest surface rainfall.	Guo et al. (2013), Guo et al. (2015)
Chinese Weather Modification Project (2001-2005),	For Hygroscopic seeding, particles smaller than 1 micron are ideal compared to particles larger than 5 microns. Extra area effects of seeding	Guo et al. (2015), Guo and Zheng (2009), Wang et al. (2019b)
Chinese cloud modification project (east coast) using radar, aircraft, radiosonde	Cloud suppression through hygroscopic seeding ZY-1NY flares are composed of potassium chloride (KCl) and calcium chloride ($CaCl_2$)	Wang et al. (2019a)
Randomized convective cloud seeding experiment in extended areas in Cuba (EXPAREX)	Radar, aircraft, 20 experimental units	Martinez-Castro et al. (2011)
Indonesian Rain enhancement program	Ground-based generators, hygroscopic seeding over the mountain	Renggono et al. (2022)
Cloud Seeding Operations in the Central Plateau of Iran	Rain gauges, 1998-2015 operations, statistical evaluation, runoff calculations	Zahraie et al. (2021)
Evaluation of hygroscopic cloud seeding by a hybrid microphysics scheme.	Simulations indicate that appropriate CCN size and seeding agents over 40-60 km2 are the most effective ways to increase rainfall.	Lin, Chung et al. (2023)

Effect of hygroscopic seeding on warm raindrop formation	Removing small particles from commercial flare size would greatly improve seeding efficiency.	Segal, Khain et al. (2004)
Impact of hygroscopic flare seeding on cloud-droplet growth: Queensland Cloud Seeding Research Program field campaign.	Seeded clouds of initial droplet spectra (cloud base 300–600 m) showed an increase in drop diameter and tail size over 20 μm within a given aerosol regime.	Tessendorf et al., (2021)
The impact of hygroscopic seeding on precipitation initiation by hybrid bin microphysics parcel model.	Hygroscopic seeding is only effective if the seeding particles are coarse, while water-soluble background coarse particles reduce the efficiency of seeding.	Geresdi et al., (2021)
Hygroscopic Seeding and Mixed-Phase Microphysics in Convective Cloud Interaction by Lage eddy UCLALES-SALSA model	Highlight the importance of mixed-phase processes in mediating the effects of hygroscopic seeding on rainfall.	Tonttila et al., (2022)
Calculations Pertaining to Hygroscopic Seeding with Flares from south African seeding experiment.	Warm-rain process can be accelerated significantly by Hygroscopic Seeding particles.	Cooper, Bruintjes, & Mather, (1997)

Israeli Cloud Seeding Experiment:	Israel 1: February 1961 - April 1967, 364 experiment days, 15% enhancement (root double ratio statistic) Israel 2: Seeding increased precipitation by 3 and 18% in the combined North and Catchment regions with the significance thresholds of 2.8 and 1.7%. Israel 3: during 1975–95, southern Israel did not show a beneficial effect of seeding. Israel 4: Randomized cloud seeding experiment, 2013 to 2020. 1.8% increase, p value = 0.4, and 95% confidence interval of (−11%, 16%)	Gabriel & Baras, (1970) Gagin & Neumann, (1981) Rosenfeld (1998) Benjamini et al., (2023)

Supplement B: Ground-based instruments, radar and ARG network and airmass trajectory

Instruments used for Ground Campaign at Solapur			
Instrument/Make	Parameters	Accuracy/Range	Reference (Relating to CAIPEEX)
Microwave Radiometer Profiler (MWRP) Radiometrics Inc.	Vertical profile of temperature and humidity and liquid water. Other parameters include PW, LCL height, CAPE, CINE, freezing level, inversions, cloud base, and cloud vertical structure. (Used RAIOB software for various estimates)	Liquid Nitrogen (LN2) calibration as factory standard TB ±0.2°C T ±0.5°C@25°C RH ± 2 % Pb ± 1.5 mb	Balaji et al. (2017) Patil et al. (2022)
Aethalometer Magee Sci., Inc.	BC aerosol mass concentration	Detection Limit (1 hour): <0.005 µg/m3 Accuracy: 1 ng/m3	Safai et al. (2013) Jayachandran et al. (2022b)
Ion Chromatograph Metrohm IC,850	PM1 and PM2.5 chemistry	0.005 to 0.1 µg/m^3	Nesterenko (2001)

CCN counter DMT Inc.	Cloud Condensation Nuclei at different supersaturations (Range: 0.1-1.2%)	Size resolution = 0.5 µm	Varghese et al. (2021) Jayachandran et al. (2020)
Scanning Mobility Particle Sizer (SMPS) TSI Inc.	Aerosol size distributions	Size range: 15 nm to 700 nm	Varghese et al. (2020) Jayachandran et al. (2020)
Impact Disdrometer Distromet Ltd.	Raindrop size distribution	Drop size range: 0.3 - 5 mm Accuracy: ± 5 % of measured drop diameter	Raut et al. (2021) Konwar et al. (2022)
HTDMA Brechtel Inc.	Hygroscopicity of aerosols	RH range: 2-93% RH accuracy=0.5% Particle size: 0.01-2 µm	Jayachandran et al. (2022a)
Sunphotometer	AOD	Precision: 1-2 % Resolution: 0.01 W/cm2@305nm	Soyam et al. (2021)
SODAR Scintec Inc.	Wind profiles from 10 m to 200 m	Accuracy of wind speed (u,v): 0.1-0.3 ms-1 w speed: 0.03-0.1 ms-1	Resmi et al. (2019)
Micro rain radar METEK Inc.	Raindrop size distributions	Drop size range: 0.2 - 6 mm vertical resolution: 200 m	Raut et al. (2021) Konwar et al. (2022)
Wind profiler Astra MW Ltd.	Wind profiles between 300m to 10 km	Height resolution: 120 m Wind speed accuracy: 1 ms-1	Konwar et al. (2022) Solanki et al. (2022)
All in one weather sensor	Temperature, winds, pressure, rainfall, RH	T ±0.3°C (@ +20°C) P ±0.5 hPa (@ 0° to 30°C) ±1 hPa (@ -52° to +60°C) RH ±3% RH (@ 0 to 90% RH) ±5% RH (@ 90 to 100% RH) U ±0.3 m s-1 or ±3% Wind Direction ±3° Precipitation Accuracy Better than 5%	Chowdhuri et al. (2021)
50 m instrumented tower for surface energy,	(all in one weather sensor, Sonic Anemometer, CO_2/H_2O		Chowdhuri et al. (2021)

radiation and momentum flux measurements Licor Inc. (CO2/H2O analyser) Gill Inc. (Sonic)	Analyzer, Pyranometers, Soil moisture and temperature sensor)		
Radiosonde MW31 radiosonde system from Vaisala, Oyj with RS-92 SGP radiosondes launched from the 12 m high terrace	Winds, temperature and RH	ascent rates of approximately 5-6 m/s were maintained as per the WMO guidelines. Data were acquired at 3 seconds intervals (50 to 60 meters)	Thomas et al. (2018)
Tipping bucket Rain gauge (TBRG, model TB4/0.2 mm) network Supplied by M/S Phame Enterprise	High resolution 1 min rainfall data, Quantitative Precipitation Estimation, Radar validation, Seeding Signature.	Tipping resolution of 0.2 mm. Data is acquired at every 1 min interval. Remotely transmitted to the data server through a mobile network.	Gayatri et al. (2022)
C-band radar (Selex/Leonardo Inc.)	polarimetric measurements of precipitation and clouds, Doppler winds, tracking the cloud systems	Operating frequency: 5.625 GHz, Tx Power: 250KW, Klystron based. ~1° Beamwidth. Calibrated periodically for power in H and V channels, system noise, and terrestrial noise. Vertical scans during drizzle are conducted from time to time for ZDR calibration.	Raut et al. (2020) Samanta et al. (2021a, 2021b, 2023)

B1. Aerosol observations at the ground site

Aerosol and cloud condensation nuclei (CCN) observations at the ground site exhibited a significant reduction in the CCN concentrations to less than 1000 cm^{-3} and activation fraction (AF) to ≅ 0.15 (from ≅0.55) at 0.3 % supersaturation (SS) during the peak monsoon. After that, it increased to ≅ 0.32 (Jayachandran et al., 2020). The aerosol size distribution (ASD) was monomodal with a geometric mean diameter of ≅ 85 nm, before the monsoon, while multimodal ASD was found during the monsoon and could have an impact due to the different

aerosol sources and scavenging/regeneration mechanisms. Critical activation diameters at 0.3 % SS were ≅ 72, 169, and 121 nm before, during, and after the monsoon, respectively (Jayachandran et al., 2020), indicating transport of cleaner air and larger sea salt particles from the Arabian Sea during the monsoon. The nucleation mode aerosols were consistently observed during the dry conditions and were also attributed to the nucleation of aerosol particles (Varghese et al., 2020). The apparent formation rates of nucleation mode aerosols varied between 0.2 to 10.0 cm^{-3} s^{-1}, and the growth rates from 1.2 to 13.8 nm h^{-1}. The nucleation events were less frequent during the core monsoon period in August and more prevalent in post-monsoon. The CCN efficiency and hygroscopicity were generally high during the daytime dry periods of monsoon (Jayachandran et al., 2022a), as seen from the Hygroscopic Tandem Differential Mobility Analyser (HTDMA) measurements on the ground. The accumulation/Aitken mode aerosols co-varied with equivalent black carbon (eBC) aerosols observed with an aethalometer during dry/wet continental conditions. December–May (dry), the mean black carbon (BC) was 4.3±1.2 μg m^{-3} as compared to the wet period between June–October (wet) where the mean BC was 1.0 ± 0.15 μg m^{-3} (Soyam et al., 2021). In general, BC levels tended to peak in the morning, and low values were noted in the afternoon. For the dry period, the absorbing Angstrom exponent (AAE) value was 1.36 ± 0.16, whereas, for the wet period, it was about 1.10 ± 0.22. The source apportionment of BC showed the dominance of fossil fuel burning throughout the year and was high during the wet period, accounting for around 89±11 % of total BC. In contrast, during the dry period, a significant contributor to BC was found to be biomass burning which made up about 30±14 % of total BC. The intraseasonal variations of BC largely depended on the wet scavenging during the monsoon and the rapid recharging of carbonaceous aerosols from local aerosol sources (Jayachandran et al., 2022b). The predominance of organic carbon was noted with a (ratio of organic carbon and elemental carbon) OC/EC ratio>5 during the dry period and that reduced to 3.5 with the onset of monsoon. However, OC/EC ratios increased during the break periods of monsoon with dry conditions, and the primary organic carbon showed a strong association with the BC mass.

B2. Airmass trajectory (HYSPLIT) and aerosol vertical profiles from CALIPSO satellite data

Analysis of 227 CALIPSO overpasses from January 2018 to December 2019 at the closest proximity to Solapur station (within ± 1°) are presented in Figure B2. The vertical distribution of the aerosol extinction coefficient and the aerosol types are obtained from level 2 aerosol

profile and Vertical feature mask data. Aerosol extinction peaks during MAM and monsoon months (July-Aug). The peak during monsoon can be attributed to the contribution from convective transport and mid-tropospheric advection from source areas in the Middle Eastern land areas and Thar desert (e.g. the year 2018). The bulk of the aerosol in the lower atmosphere is continental dust.

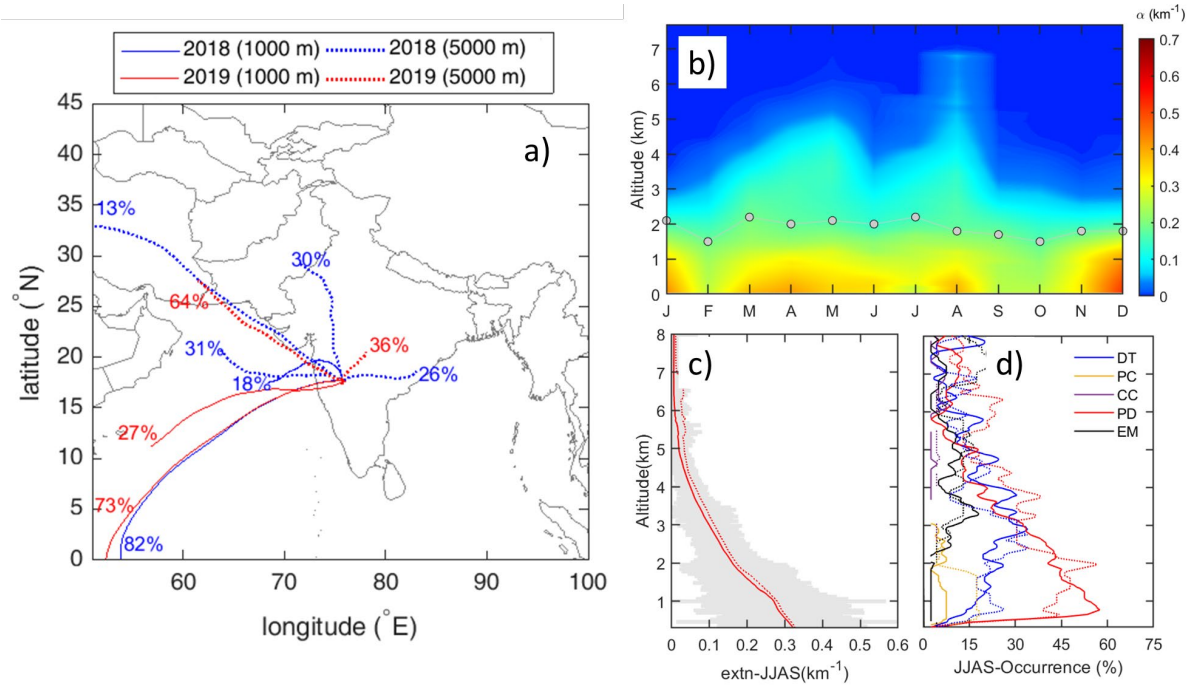

Figure B1. The seasonal mean of HYSPLIT -five-day backward trajectory path (a) at 1000 m (solid blue line) and 5000 m (solid red line) during 2018 and 2019; The vertical distribution of aerosol extinction coefficient from CALIPSO measurements during 2018 – 2019 (b). The solid grey-encircled marker indicates the composite monthly total number of profiles /10. Vertical distribution of aerosol extinction coefficient (c) and the occurrence of aerosol subtype (d) during the monsoon seasons of 2018 (solid line) and 2019 (dashed line). The aerosol subtype in legend represents dust (DT), polluted continental (PC), clean continental (CC), polluted dust (PD), and elevated smoke (EM). Concentrations of other aerosols namely, marine and dusty marine, are negligible and not included in this figure.

B3 C-Band radar

C-band radar was installed at the center of the seeding area at Solapur. Radar operations in general focus on; a selection of areas for seeding, cloud, and precipitation monitoring during the seeding and documenting the variability in precipitation. The radar was operated with different volume scan strategies with a temporal resolution of 6 minutes during the randomized seeding and 10 minutes during research scans. The elevation angles were for PPIs: 0.5, 1.5, 2.5, 3.5, 4.5, 5.5, 7, 8.5, 10, 12.5 and azimuth angles for RHIs: 0, 30, 60, 90, 120,

150. The seeding scan strategy has given a high temporal dataset during the randomized seeding operation.

CFAD analysis

The Contour Frequency by Altitude Diagram (CFAD) for each of the 151 seed / 125 no-seed samples, 2 hours (i.e 13 scans, each scan with 10 minutes intervals; 1963 scans in the seed 1625 scans in no-seed) of radar data, starting from seed/no seed case time, are taken for this analysis. Note that the seed/no-seed locations are randomly distributed based on the clouds selected for the randomization experiment.

The radar reflectivity data in polar coordinates is converted to Cartesian coordinates using TITAN (Dixon and Wiener, 1993) with 1 km horizontal and 0.5 km vertical resolution for all the radar regions. The clouds are selected within a 100 x 100 km^2 region whose center is at seed/no-seed locations, and this region is again divided by 4 boxes of 50x50 km^2 one in each of south-east, north-east, north-west and south-west directions from seed/no-seed, location. Figure 10 shows the results of boxes in a downwind direction (southeast and northeast boxes). All the data from seeding time to 1-hour duration are included in this analysis.

The occurrence of radar reflectivity values at 1dBZ bin interval is counted as a function of height (0.5 km interval) for all profiles of seed and no-seed cases. Each of these values is normalized to total occurrences of all the dBZ bins at all the heights so that the sum of entire values in Figure 10a (seed cases) or 10b (no-seed cases) equals 1. The average reflectivity profile (average_reflectivity in dBZ) and the percentage of several dBZ values (> -10dBZ) at each height (data presence) are also shown in the figure. The numbers mentioned in the boxes within the figures are the percentage of occurrences within those small boxes, and as mentioned before, it is 100% if the box is drawn for the full figure.

B4. Rainfall estimation from the radar and collocated ARG network

The method applied for each seed/noseed case evaluation by ARG and by radar is described here. In order to assess the effect of seeding on rainfall, ARGs in the downwind area of the seeded location within 10 x 10 km^2, 25 x 25 km^2 and 50 x 50 km^2 area are considered. An example of such an investigation is given in Figure B2. The radar location (red circle in Figure B2a), seeded location (*), ARG locations (dots) and 25 km radius circle (black color) show the rain gauges covered under the seed event. In Figure B1b, this 25 km circle is zoomed to

show the rain gauges falling in a downwind direction. The numbers in Figure B2b indicate the ARG locations and their ID numbers. The center of the box is the seeded location. To evaluate the effect of seeding (or noseed), the rainfall in the downwind direction is investigated. The following method is applied to evaluate seeding effect: (i) identify the ARGs in the downwind direction from the seeding location, (ii) calculate a 10-minute accumulation of rainfall from each ARG and get that data for 120 minutes *[13 data points including seed time]*, (iii) Average this time series from all the ARGs in that area. (iv) Repeat point numbers (i), (ii), and (iii) for each case of seed/no-seed event.

Similarly, for rainfall estimation from radar data (i) From each volume scan (every 10 minutes), get 1 km CAPPI. This contains 500 x 500 pixels, each pixel is of 1x1 km^2 area, (ii) calculate rainfall using selected Z-R relationship, (iii) Extract the radar-derived rainfall data for each seeding location and for each of ARGs. While selecting the radar pixels for each ARG location, 3x3 (i.e. 3km x 3km area aloft the ARG) pixel average around the ARG location is used (iv) prepare a time series of 10-minute rainfall for 2 hours from seed/no-seed time and average it for all the ARG locations *[again 13 points of data]*. Thus, every 10 minutes after seeding, average rainfall in the downwind direction (mm of rainfall in 10 min) is found using ARGs and Radar measurements for comparison. The seeded and unseeded cases are separated. These rainfall values for every 10 minutes are accumulated for (i) all seed cases (ii) no seed cases. The analysis presented in the study is for 10x10 $km^{2,}$

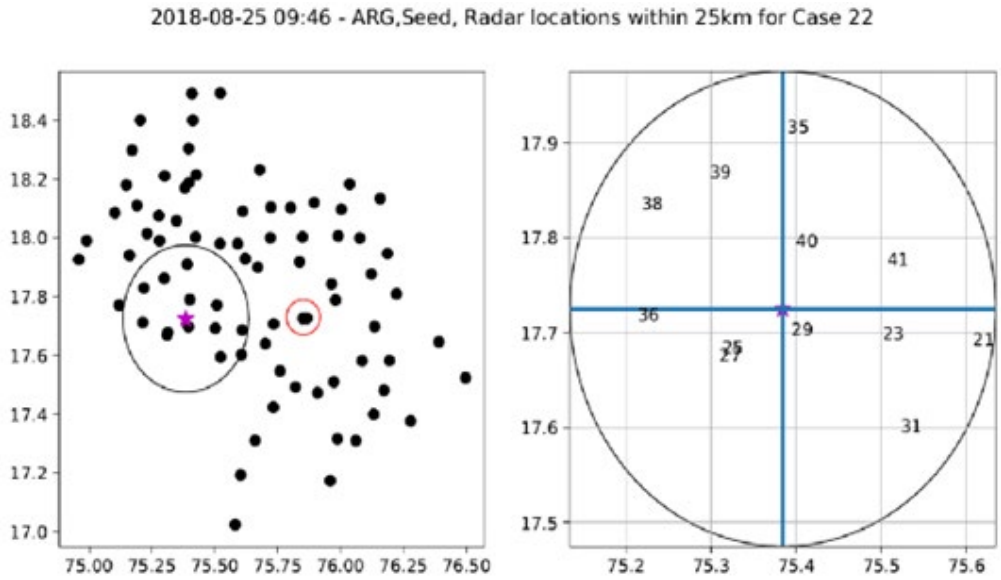

Figure B2: (a) An example giving information on the location of seeding (Star symbol), ARG locations (solid circles) radar location (red circle), and (b) shows how rain gauges are considered for the analysis of 25km radius (i.e for 50x50 km^2 area). The ARGs in the SE sector are considered for calculating rainfall in a downwind direction.

B5. Warm layer depth and mid-tropospheric RH

Figure B3a highlight the relationship between the warm layer depth and the cloud droplet effective radius from in situ measurements, cloud-resolving model data for different conditions, and large eddy simulation (LES) results for different moisture and CCN conditions (Gayatri et al., 2022). The linear relationship holds as the moisture increases in clean and polluted conditions. Deeper warm layer clouds may grow into the mixed phase region with large enough drops so that drop freezing may occur. The temperature inversion at 6-8 km is a limiting factor for the vertical growth of clouds; however, it was found that mid-tropospheric (2-6 km is used from radiosonde) relative humidity (RH) >60 % would favor deep cloud growth (Malap et al., 2021). A relationship between the mid-tropospheric RH (from radiosonde) and cloud depth (from radar) over the study region (Figure B3b) shows a wide range of cloud depths for different RH, the deep clouds (>6 km cloud depths) are above 40 % RH and in the 60 percentile.

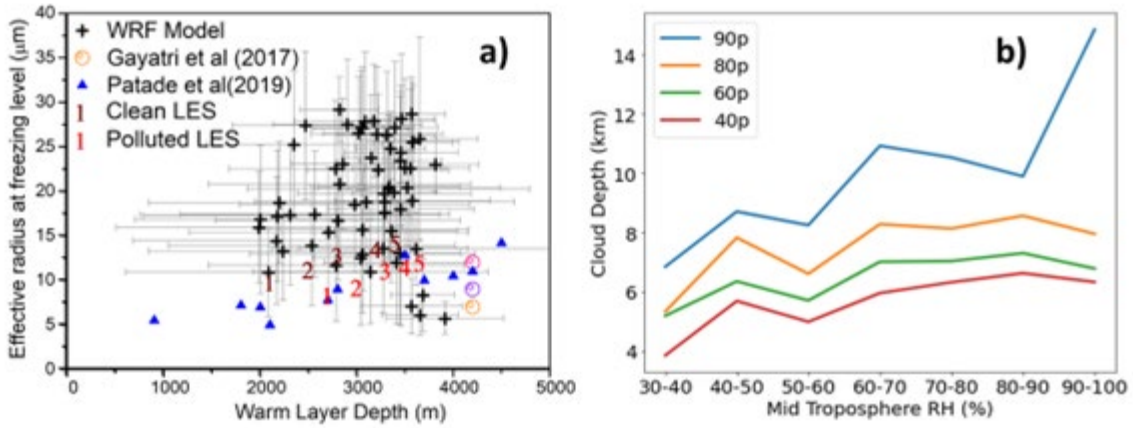

Figure B3. a) Warm layer depth and effective radius at the freezing level from cloud-resolving model data (A: CCN=100 cm^{-3}; B: CCN= 1000 cm^{-3}; C: 3000 cm^{-3}) of Gayatri et al., (2017), from in situ measurements (blue triangle; Patade et al., 2019) and from large eddy simulation (LES) for clean and polluted conditions under increasing humidity (1-5 indicates low (-20 % RH) to high (+20% RH) humidity concerning observations presented in Gayatri et al., (2022). The plus symbols with error bars indicate high-resolution (1 km) cloud-resolving model (CRM) derived data from the study region during the monsoon season. b) The relationship between the mid-tropospheric RH and cloud depth is given in percentile from several radiosonde observations during the JJAS and respective cloud depth estimates from radar data.

Supplement C:

C1: Aircraft Instruments and flight plans

Cloud physics measurements were conducted with a Research aircraft (RA, Beechcraft B200), fully equipped with aerosol-cloud-precipitation measurement systems, vertical velocity, and other state parameters, etc. as shown in Table C1. This aircraft makes vertical profiles of clouds before and after the seeding mission is completed by the seeder aircraft or carries out seeding and vertical profiling of clouds per set criteria for cloud profiling (Figure C1) by making passes across clouds at specified altitudes above the cloud base. Flares are fitted to the racks on the wings. The randomization experiment was always done with a specific flight plan. The seeding regions are selected based on radar observations and are usually away from any other hygroscopic seeding that has taken place.

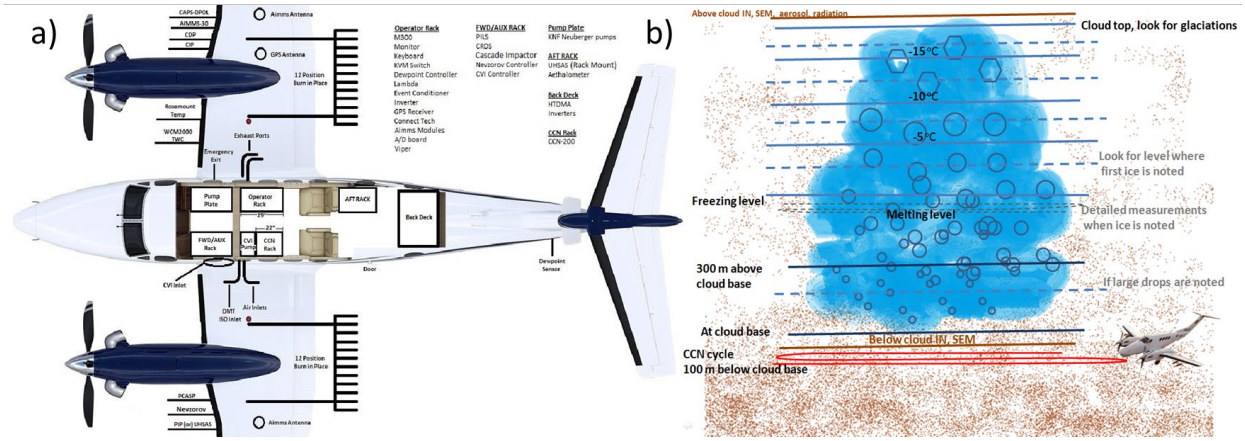

Figure C1 Configuration of instruments in the research aircraft (Image courtesy: Aircraft provider Weather Modification Inc. WMI, USA), b) Cloud profiling strategy for a convective cloud (redlines indicate the CCN cycle 100 m below cloud base, blue thick lines indicate the cloud passes at specific altitudes with research aircraft, dashed lines are required penetrations for specific purposes as indicated such as to find the first ice or the raindrop formation/ documenting the melting layer, etc.).

Table C1 Instruments on the aircraft

VARIABLE	INSTRUMENT	RANGE	Accuracy	Reference
Wind velocity	Air Data Probe Aircraft Integrated Meteorological Measurement System	High resolution	Differential pressure sensors	Beswick et al. (2008)

	(AIMMS-20, ADP, IMU, WAAS DGPS, CPM)		accuracy 20 Pa + 0.05% of reading	
Air temperature	Rosemount temperature probe	-50°C to +50°C	+/- 0.25 C	Khelif et al. (1999)
Dew point temperature	Chilled mirror aircraft hygrometer	-40°C to +60°C	+/- 0.20 C	Busen et al. (1995)
High-resolution cloud droplet measurements	Cloud Droplet Probe – CDP 2	Particle by particle 2 to 50 µm	2-3 um resolution	Lance et al. (2010, 2012)
Cloud condensation nuclei (CCN)	CCN-200 Dual column CCN counter	0.1 to 1.2 % SS		Roberts and Nenes (2005), Rose et al. (2008)
Polarization measurements with particle probe, with particle-by-particle arrival information	Cloud, Aerosol, and Precipitation Spectrometer (CAPS-DPOL), With K-tips for reducing shattering effects	Aerosol particle and cloud hydrometeor size distributions from 0.51 to 50 µm Precipitation size distributions from 15 µm to 960 µm With 15 µm resolution		Baumgardner et al. (2011)
Nucleation mode aerosol spectrometer	High flow Differential Mobility Analyzer (DMA)	0.01 to 0.5 µm		Collins et al. (2002)
Accumulation and coarse mode aerosol spectrometer (particle by particle)	Ultra-High Sensitivity Aerosol Spectrometer (UHSAS)	0.05 to 1 µm	99% counting efficiency	Cai et al. (2013)
Aerosol Size Distribution	Passive Cavity Aerosol Spectrometer (PCASP)	0.1 to 3 µm		Strapp et al. (1992)
Cloud droplet/particle size distribution	Cloud Imaging Probe (CIP)	15 to 930 µm	15 µm resolution	Baumgardner et al. (2001)

Precipitation imaging and size distribution	Precipitation Imaging Probe (PIP)	100 to 6000 µm	100 um resolution	
Liquid water content	Hotwire Liquid Water Content (LWC)	0 to 3 g/m3		
Refractory Black carbon r(BC) mass concentration, particle size	Single particle soot photometer - extended range (SP2-XR)	BC in the aerosol, in spite of mixing state down to 50 nm		Baumgardner et al. (2004)
Aerosol Counting, Composition, Extinction, and Sizing System (ACCESS) on the seeder aircraft	Mixing Condensation Particle Counter (MCPC),Optical Particle Counter (OPC), Multi-Channel Chemical Sampler (CHEM), Single channel TAP(450, 525, 624 nm)		https://www.brechtel.com/products-item/aerosol-counting-composition-extinction-and-sizing-system/	
Particle Into Liquid Sampler (PILS) 7 minute sampling using PILS. Analysed offline using IC	Major inorganic cations and anions and WSOC	0.005 to 0.1 µg/m^3		Orsini et al. (2003)
Aerodyne MiniHigh-resolution Time of Flight Aerosol Mass Spectrometer (MiniH-TOF-AMS)	Aerosol chemistry and tracking the seeding signature		Quantitative mass concentrations of the major non-refractory particles of submicron size.	DeCarlo et al. (2006)
Wideband Integrated Bioaerosol Sensor (WIBS) dual-wavelength	Bioaerosol measurements	size range 0.5 - 30 microns and concentrations from ~500 - 5000 /liter		

fluorescence spectrometer				
Air Data Probe Liquid water content Cloud seeding score	Cloud Water Inertial Probe (CWIP): gives LWC, air velocity and cloud seeding score	0 to 3 gm^{-3}	-5% (10um drops) to -20% (<5um drops)	

Inlets

Diffuser inlet installed in laminar flow outside of the aircraft boundary layer Aerosol measurements	Isokinetic aerosol inlet	> 20 lpm	N/A	CCN, DMA, PILS, Aerosol Filter Collection, WIBS, mini- Aerosol Mass Spectrometer (mini-AMS and SP2.
Analysis of cloud residue particles, their size distribution and black carbon mass	CVI inlet	Droplet diameter cut size range 6-14 µm	>95% sampling efficiency for residuals from 0.01 to 6.0 um	SP2-XR, filter sampling, WIBS, mini-AMS
Gas measurements	Reverse flow inlet	CH_4, CO_2, CO and H_20		CRDS gas analyser

C2: Aircraft data processing

Most of the aircraft instruments were from Droplet Measurement Technologies LLC and rapid maintenance and data checking and processing service was taken from OEM to meet the daily demands. PCASP Concentration has been corrected to account for uncertainty resulting from offsets in PCASP flow meter calibration. CCNC utilizes a constant pressure inlet that maintains the inlet pressure at approximately 700 mb. Measurements when the ambient pressure, Pamb > 700 mb, are corrected using the factor Pamb/700. Measurements when Pamb < 700 are screened out. Data was also screened out for 60 seconds after each change in supersaturation (SS). Further filtering of data was done for sudden changes during the SS cycles. CIP/PIP data is screened out, as the diode voltages fall below 1.5 V. CIP/PIP Splashing/shattering artifacts are removed from the image data (Field et al. 2003; Korolev and Field 2015). CIP The first three channels (15 - 75 µm) and channels (11 - 62) are removed when computing the bulk parameters to represent drizzle-sized drops. Out-of-focus drops are detected

and resized (Korolev 2007). The bulk parameters are computed using the size derived as the size that a circular drop would have given the measured area of the image. The CIP image measurements were evaluated to determine the optimum interarrival time to use as a threshold. LWC-300 – data was processed to remove the influence of heat losses by convection while in the cloud before deriving the LWC. Figure C2 gives different parameters from the AIMMS data probe.

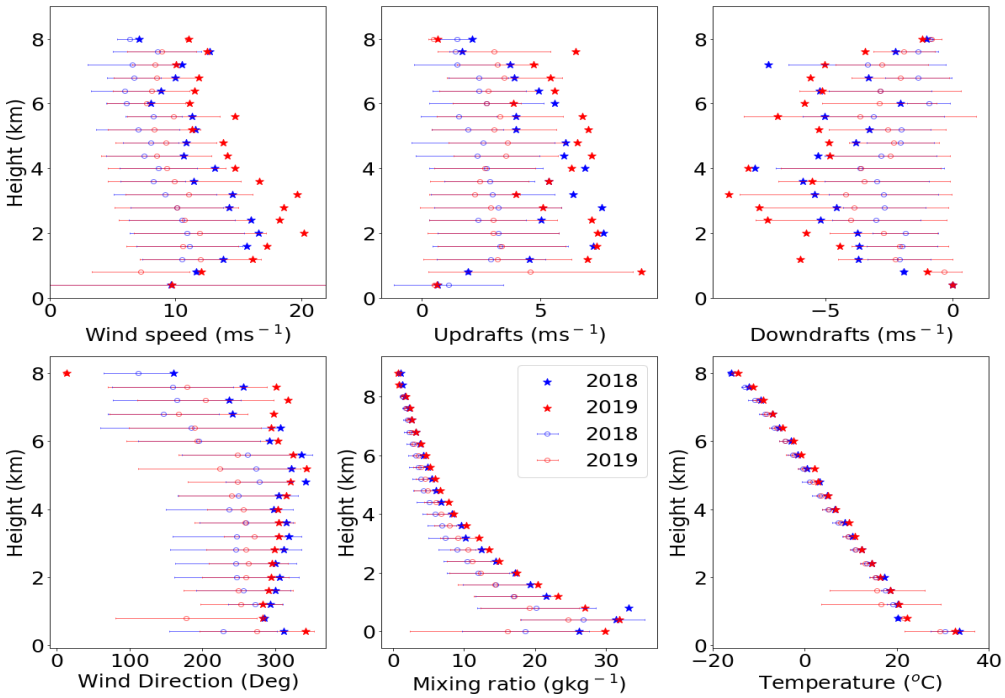

Figure C2: Average value of wind speed (a), updraft (b), downdraft (c), wind direction (d), water vapor mixing ratio (e), and temperature (f) from aircraft observations at different altitudes. Updrafts and downdrafts are from within cloud observations screened by a droplet number concentration of more than 20 cm-3.

C3: Flare characterization

The hygroscopic seeding flares are characterized using a special flight plan during the experiment; aerosol size distribution from the flare burning was documented by a seeder and research aircraft flying along a line and with a 100 m distance between the two aircraft. The experiment was done at the end of the campaign due to the requirement of dry conditions. The specific design of the flare testing flight was done with the following details: fly into the wind (or against the wind); Below the cloud base and above the boundary layer, Fly below 700 mb altitude; sample seed plume always along a line; CCN Column A at 0.2% and column B at 0.6%; filter samples (background, engine exhaust and flares); Repeat the exercise at two altitudes; Burn two flares on each wing and then 4 flares on each wing. The figure gives the details on the flight track.

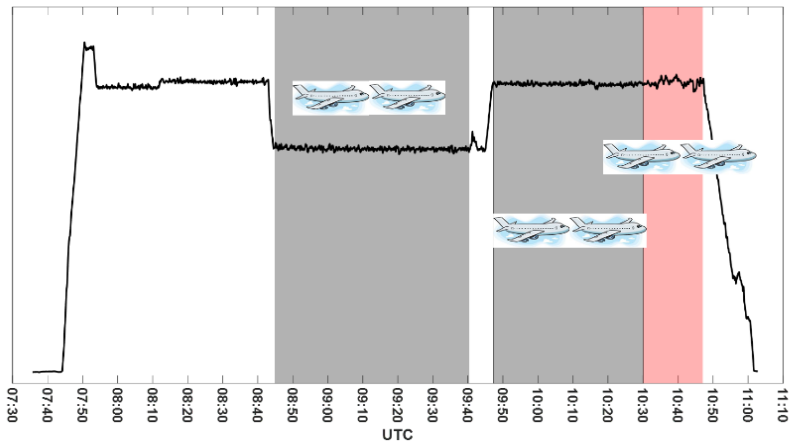

Figure C3. Flight track of the seeding flare evaluation flight

Both research aircraft have sampled aerosol with UHSAS, PCASP, SP2-XR, and CCN counter. The seeder aircraft was burning flares and the research aircraft initially sampled the background aerosols, then followed the seeder aircraft to sample the aircraft exhaust, seeding flares when two flares and four flares were burnt. The measurements were made at ~1500 m AMSL. The ambient temperature, wind speed, wind direction, and updraft were about 21.6 ± 0.21 ºC, 7.7 ± 1.1 m s^{-1}, 93.2 ± 10.5 º, and -0.18 ± 1.6 m s^{-1}, respectively.

Lognormal fits of different aerosol size distributions in three modes are derived for the data presented in Figure 6 of the manuscript. The table gives the mean radius, spectral width, and number concentration in three modes.

Lognormal fits of different aerosol size distributions for background and seeding experiment

	R1 (nm)	σ1	N_mod1 (cm-3)	R2 (nm)	σ2	Conc2 (cm-3)	R3 (nm)	σ3	Conc3 (cm-3)
Background (B)	23.16	2.27	10493.06	166.05	1.66	512.43	1129.52	1.81	27.68
B +Exhaust (E)	38.64	1.78	7542.22	176.73	1.72	500.61	1214.31	1.81	31.26
B+E+ 2Flare	69.08	1.23	20280.96	184.40	1.66	538.41	1276.00	1.83	33.21
B+E+ 4Flare	60.04	1.27	35341.14	161.93	1.66	990.44	1098.00	2.24	51.68

Supplement D Randomization and evaluation procedure

D1. Randomization procedure

The same randomization procedure used in the South African, Mexican, and Australian experiments is used. Two sets of decision envelopes are made, one at the radar site and another in the aircraft. This procedure is followed to ensure that no project personnel has prior knowledge of the contents of the envelopes. The radar envelopes contain either a 'seed' or a 'no-seed' decision. The aircraft envelopes also contain either a 'yes' or a 'no' decision. The seeder aircraft makes a flight near the cloud base and 1000 ft above the cloud base during the procedure. In the first cloud pass, it will register the updraft and liquid water content. If the cloud is growing and non-precipitating, the case is declared and both the radar operator and the pilot will open an envelope and will execute the seed or no seed action based on the decision from the envelope. If the decision is to seed, the pilot will burn 2 flares at a time, two on each wing, while flying below the cloud base and through the updraft as much as possible. A maximum of 4 flares is used on any one case. The flares take approximately 4 minutes each to burn completely. If the decision is no-seed, the pilot flies the mission in exactly the same manner as if the decision were for seeding, up to a maximum seeding time of 4 min. The pilot will record flare burn times. The pilot also notes the start and end times for each case and each seeding event in the pilot logs.

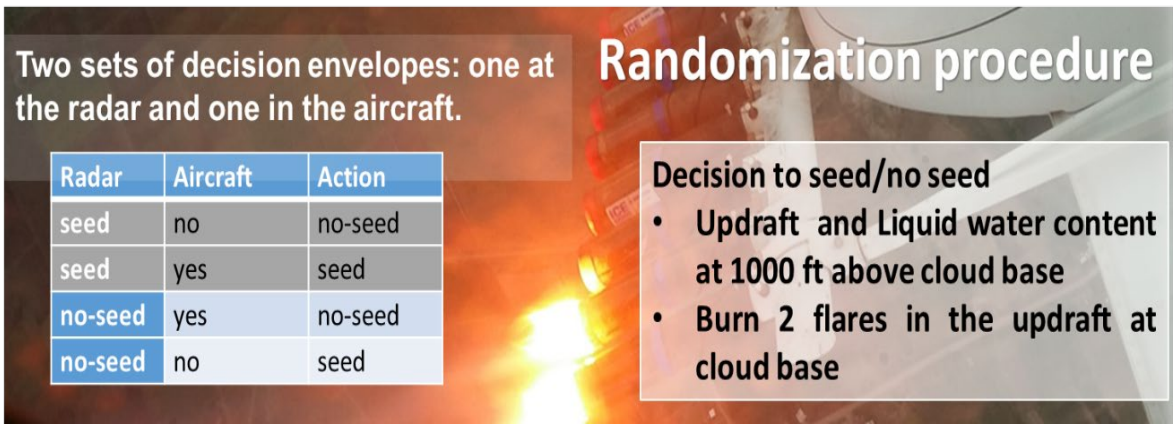

Figure D1 Decision table for the randomization experiment

D2. Bootstrapping method

From the rainfall data for the 100 km^2 downwind area, the accumulated rainfall from ARG and the radar is found for 2 hours after seeding. There are 104 seed and 91 no-seed samples

in the downwind area with radar observations. However, ARG data was available with 44 seed and 42 no-seed samples. The mean and standard deviation of rainfall from rain gauges and corresponding radar locations of seeded cases are 0.5±1.57 and 0.63±0.99 mm, respectively. On the other hand, for the non-seeded cases, these numbers are equal to 0.36±1.7 and 0.51±1.14 mm, respectively.

We analysed two sets of data (44/42 seed/noseed ARG, and 44/42 seed/noseed radar) with Bootstrapping method to check the robustness of the sample mean. It is not known beforehand whether, for such a scenario, the assumption of Gaussianity is true. Hence, an alternate strategy is to generate the distribution of the mean rainfall values from the data itself through random resampling (Brownlee 2019). In our case, we randomly choose samples and repeat the process 1000000 times. A comparison of the distribution from the ensemble of ARG and radar datasets is given for seed and no-seed samples (Figure C5)

The ensemble set is also given as a box-whisker plot and the sample mean is in Figure C5. The range of the mean values is larger for the seeded cases compared to the non-seeded cases in ARG compared to the radar.

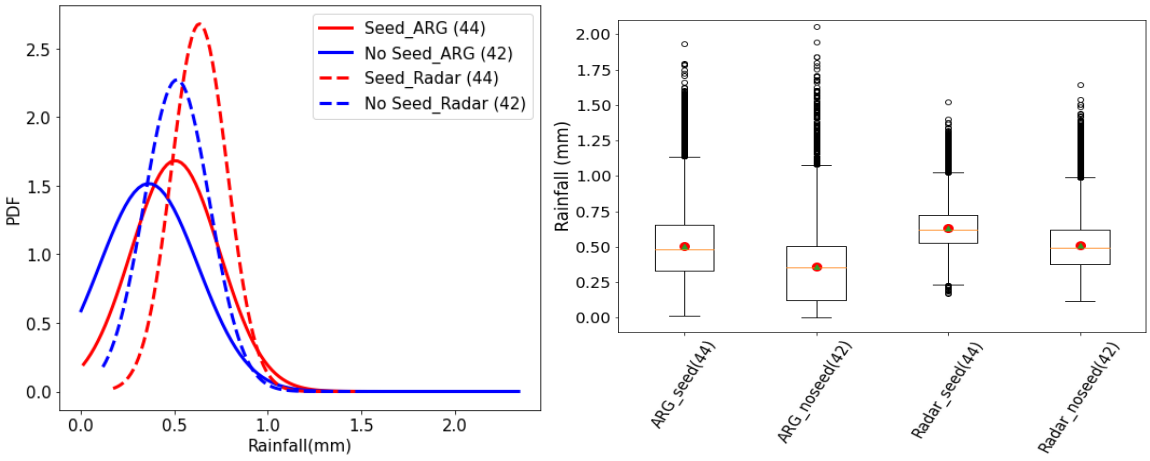

Figure D2 PDF of seed and no-seed samples from the bootstrap analysis for colocated ARG and radar for seed/no-seed samples. The number of samples used is mentioned in the legend, which depends on available ARGs. The box-whisker plots of the mean rainfall distribution were generated through the bootstrapping method, as shown in the figure. The lower and upper black lines indicate 25- and 75-percentile lines, and the red line in the middle denotes the median. The black lines show the range beyond the 75 and 25 percentiles, along with symbols showing outliers from the bootstrapped sample mean. The filled red circles show the sample mean rainfall in the seeded and non-seeded cases.

D3. Area averaged rainfall

The agreement between the radar data at ARG locations brings confidence in the radar observations. It must be noted that further site-specific disdrometer data is to be implemented in the ZR relations for different rainfall types in future studies. However, as mentioned below, the analysis gives some of the intricate uncertainties in any randomization study. We have also checked the area averaged rainfall in the 100 km^2 area with 150 seed and 122 no-seed samples. We divided the entire dataset into 4 sectors, and the figure gives the box whisker plot of data in the four sectors for the seed and no-seed datasets. The rainfall relative enhancement is noted in sectors 1 and 4. The enhancement noted in sector 4 is attributed to more samples in the 75th percentile with higher rainfall.

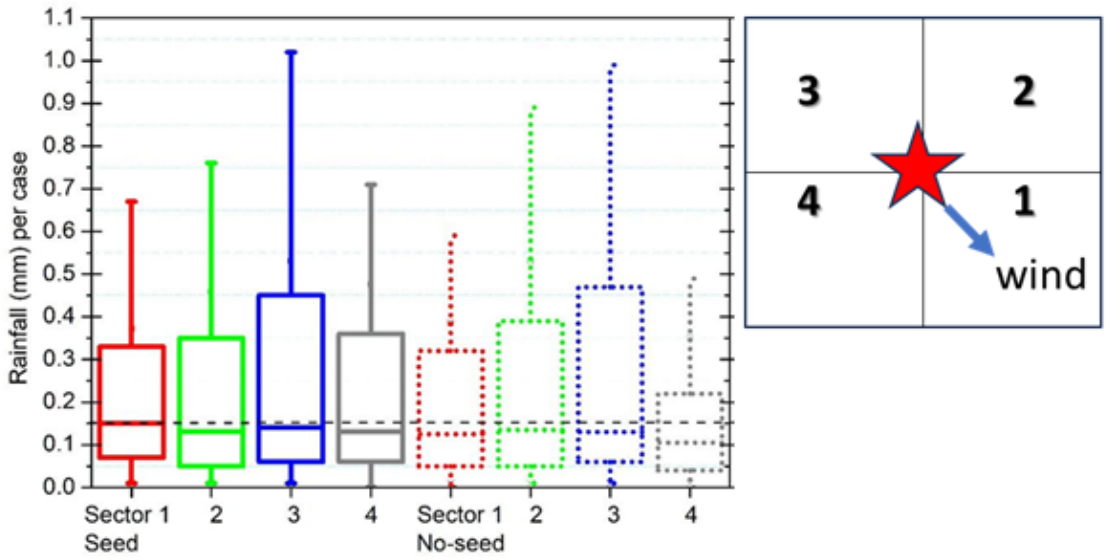

Figure D3. Box whisker plot of radar rainfall in the seed (solid box) and no-seed (dotted box) samples in four sectors of randomized seeding. The left 4 bars are for the seed sample, and the right 4 bars are for the no-seed sample. In each bar char, the middle line is the mean, the upper horizontal is the 75 percentile, and the lower horizontal line is the 25 percentile. The outliers are above the scale shown. The dashed horizontal line is the mean rainfall amount in the 100 km^2 downwind area of the seeded location.

Considering all four sectors, we may note that the overall mean rainfall is 3.12 mm per seeded sample (150 no.) and 1.82 per no-seed sample (122 no.), with standard deviations of 3.12 mm and 2.84 mm, respectively. Minimum/Median/Maximum values for the seed sample is 0.4/0.79/20.92 mm, and for the no-seed sample is 0.07/0.6/16.76 mm

We look at the QQ plot for the seed and no-seed samples in each sector, which tells us that the sample does not have a normal distribution. There are several extreme points in the dataset

for the seed sample. Meanwhile, two extreme points in the no-seed dataset are outliers indicative of natural precipitation. However, several other points of the seed sample are higher than the no-seed samples. To check this, we investigated relative enhancement in different percentiles of the dataset (Figure 10 presented in the manuscript). The contrasting behavior of the seeded sample is evident in sector 1, with many seed samples showing larger values than the no-seed sample.

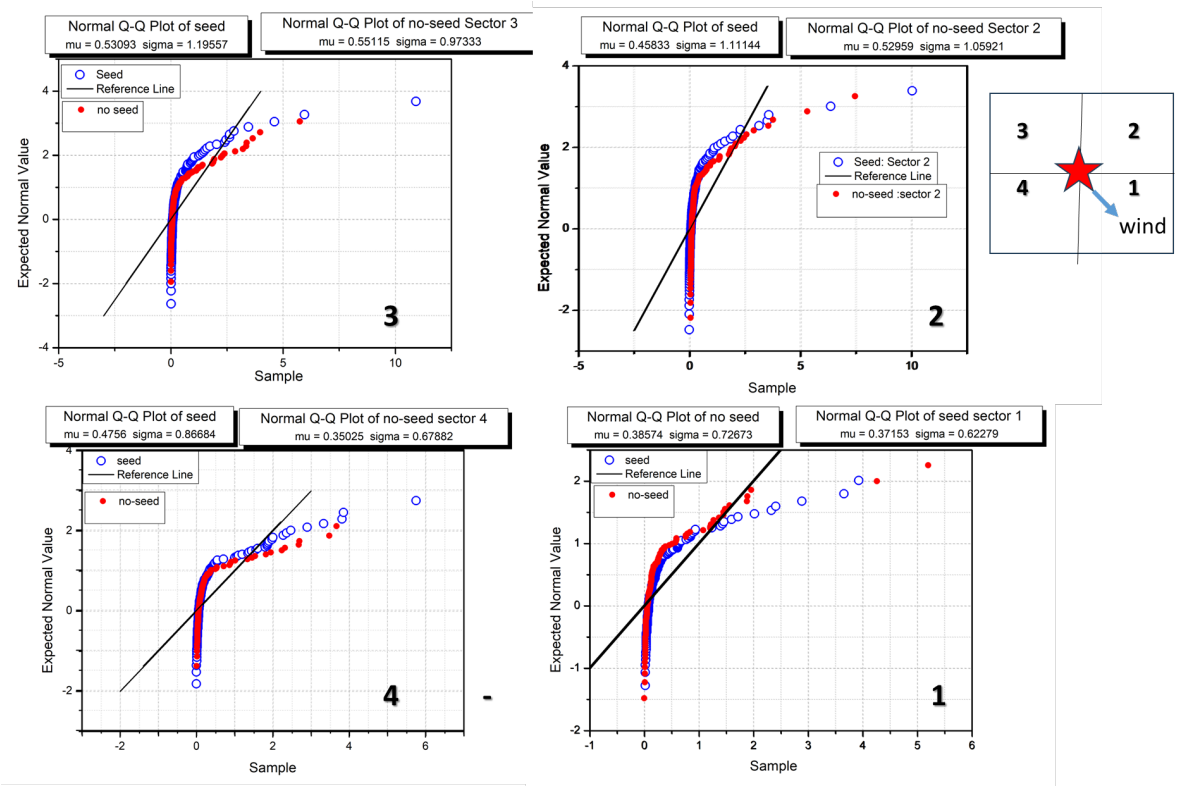

Figure D4. QQ (quartile-quartile) plot showing both datasets (seed and no-seed) in the four sectors (indicated with the seed location (star) and winds (arrow) in the upper right corner of the plot) of seeding. The black line indicates the normal distribution; all points fall on it if the dataset has a normal distribution.

D3. Quartile analysis summary together with errors in the two categories of clouds

	Isolated Clouds Category D with <30dBZ			Isolated Clouds Category E with >30dBZ		
	Seeded	**Non- seeded**	**Relative enhancement %**	**seeded**	**Non-seeded**	**Relative enhancement %**
Rain rates(mm/hr) from 1.5km elevation data	1.38±2.3	1.00±1.5	38.40	3.92±5.6	3.56±6.12	10.08
Rain Mass(Ktons)	6.63±14.02	3.74±4.72	77.38	23.11±36.21	70.19±200.82	-67.08
Precipitation Flux(m^3/s)	13.56±25.7	7.53±10.38	80.15	48.25±69.49	136.06±384.9	-64.54
Mean Area(km^2)	10.96±10.7	11.33±19.3	-3.28	21.52±20	37.88±45.7	-43.18
Precipitation Area (km^2)	18.82±17.08	11.36±9.85	65.60	32.52±36.93	62.32±86.06	-47.82
Volume(km^3)	49.89±54.21	68.02±147.43	-26.65	107.96±150.44	234.21±367.65	-53.90
Integrated liquid(Kg/m^2)	1.07±1.84	0.71±1.06	52.01	3.27±4.47	4.27±7.98	-23.42
Cloud depth (km)	2.74±2.11	2.41±1.99	13.69	4.39±3.91	4.64±3.52	-5.45
Duration (minutes)	33	26	24.50	36	35	3.12

Note: These estimates are average values for the entire cloud lifetime for isolated clouds (duration of clouds vary and are up to 2 hours) for all the seed/noseed from Category D and Category E clouds from sidebar III. Average values are also given, derived from TITAN analysis. Cloud depth is obtained by the difference between the echo top and the cloud base heights. This table is applicable for all cases that showed rain after seeding.

Appendix D List of Abbreviations

Abbreviation	Meaning
AAE	Absorbing Angstrom exponent
AF	Activation fraction
AMS	Aerosol Mass Spectrometer
ARG	Automatic Rain Gauge
ASD	Aerosol size distribution
BC	Black carbon
BIP	Burn-in-place
BL	Boundary Layer
CAIPEEX	Cloud Aerosol Interaction and Precipitation Enhancement Experiment
CALIPSO	Cloud-aerosol Lidar and Infrared Pathfinder Satellite
CAPE	Convective Available Potential Energy
CAS	Cloud and Aerosol Spectrometer
CB	Cloud base
CCN	Cloud Condensation Nuclei
CDNC	Droplet number concentration
CDP	Cloud Droplet Probe
CIP	Cloud Imaging Probe
CP	Cold Pool
CRM	Cloud Resolving Model
CVI	Counterflow Virtual Impactor
DMA	differential mobility analyser
DNS	Direct Numerical Simulation
DSD	Drop size distribution

eBC	equivalent black carbon
EC	elemental carbon
EJ	Ejectable flares
FBAP	Fluorescing biological aerosol particle
HTDMA	Hygroscopic Tandem Differential Mobility Analyser
IITM	Indian Institute of Tropical Meteorology
IMD	India Meteorological Department
IPCC	Inter-governmental Panel on Climate Change
JJAS	June to September
KDP	Specific Differential Phase
LCL	lifting condensation level
LES	Large Eddy Simulation
LLJ	low-level jet
LWC	Liquid water content
LWP	Liquid Water Path
MLD	million litre per day
MVD	Mean Volume Diameter
MWRP	Microwave radiometer Profiler
NCEP	National Centre for Environmental Prediction
OC	Organic carbon
PBL	Planetary Boundary layer height
PCASP	Passive Cavity Aerosol Spectrometer Probe
PIP	Precipitation Imaging Probe
PW	Precipitable water
RA	Research Aircraft

rBC	Refractory black carbon
RH	Relative humidity
SA	Seeded Aircraft
SEM-TEM	Scanning electron microscope and Tunnelling electron microscope
SMPS	Scanning Mobility Particle Sizer
SP2-XR	Single particle soot photometer – extended range
SS	supersaturation
UAEREP	UAE research program on rain enhancement
UHSAS	Ultra-High Sensitivity Aerosol Spectrometer
WG	Western Ghats
WIBS	Wideband Integrated Bioaerosol Sensor
WMO	World Meteorological Organization
WRF-ARW	Advanced Research Weather Forecasting model
ZDR	Differential reflectivity

Reference

Balaji, B., T. V. Prabha, Y. Jaya Rao, T. Kiran, G. Dinesh, K. Chakravarty, S. M. Sonbawne, and M. Rajeevan, 2017: Potential of collocated radiometer and wind profiler observations for monsoon studies. Atmos. Res., 194, 17–26, https://doi.org/10.1016/j.atmosres.2017.04.023.

Baumgardner, D., H. Jonsson, W. Dawson, D. O'Connor, and R. Newton, 2001: The cloud, aerosol and precipitation spectrometer: a new instrument for cloud investigations. Atmos. Res., 59–60, 251–264, https://doi.org/10.1016/S0169-8095(01)00119-3.

Baumgardner, D., G. Kok, and G. Raga, 2004: Warming of the Arctic lower stratosphere by light absorbing particles. Geophys. Res. Lett., 31, n/a-n/a, https://doi.org/10.1029/2003GL018883.

——, and Coauthors, 2011: Airborne instruments to measure atmospheric aerosol particles, clouds and radiation: A cook's tour of mature and emerging technology. Atmos. Res., 102, 10–29, https://doi.org/10.1016/j.atmosres.2011.06.021.

Benjamini, Y., Givati, A., Khain, P., Levi, Y., Rosenfeld, D., Shamir, U., Siegel, A., Zipori, A., Ziv, B. and Steinberg, D.M., 2023. The Israel 4 Cloud Seeding Experiment: Primary Results. Journal of Applied Meteorology and Climatology, 62(3), pp.317-327.

Beswick, K. M., M. W. Gallagher, A. R. Webb, E. G. Norton, and F. Perry, 2008: Application of the Aventech AIMMS20AQ airborne probe for turbulence measurements during the convective storm initiation project. Atmos. Chem. Phys., 8, 5449–5463, https://doi.org/10.5194/acp-8-5449-2008.

Brownlee, J., Statistical Methods for Machine Learning

Bruintjes, R. T., D. W. Breed, V. Salazar, M. J. Dixon, T. Kane, G. G. Foote, and B. G. Brown, 2001: Overview and results from the Mexican hygroscopic seeding experiment. Pre-prints, 15th Conf. on Planned and Inadvertent Weather Modification, Albuquerque, NM, Amer. Meteor. Soc., 45-48

Busen, R., and A. L. Buck, 1995: A high-performance hygrometer for aircraft use: description, installation, and flight data. J. Atmos. Ocean. Technol., 12, 73–84, https://doi.org/10.1175/1520-0426(1995)012<0073:AHPHFA>2.0.CO;2.

Cai, Y., J. R. Snider, and P. Wechsler, 2013: Calibration of the passive cavity aerosol spectrometer probe for airborne determination of the size distribution. Atmos. Meas. Tech., 6, 2349–2358, https://doi.org/10.5194/amt-6-2349-2013.

Chowdhuri, S., K. Todekar, P. Murugavel, A. Karipot, and T. V. Prabha, 2021: Unravelling the turbulent structures of temperature variations during a gust front event: a case study. Environ. Fluid Mech., 21, 263–281, https://doi.org/10.1007/s10652-020-09769-z.

Collins, D. R., R. C. Flagan, and J. H. Seinfeld, 2002: Improved inversion of scanning DMA data. Aerosol Sci. Technol., 36, 1–9, https://doi.org/10.1080/027868202753339032.

Cooper, W. A., Bruintjes, R. T., & Mather, G. K. (1997). Calculations pertaining to hygroscopic seeding with flares. Journal of Applied Meteorology and Climatology, 36(11), 1449-1469.

DeCarlo, P. F., and Coauthors, 2006: Field-deployable, high-resolution, time-of-flight Aerosol Mass Spectrometer. Anal. Chem., 78, 8281–8289, https://doi.org/10.1021/ac061249n

Dinevich L., S. Dinevich and B. Leskov 2008: Results of experiments and field trials on rain enhancement from clouds of various types in Moldova and Ukraine, Collected papers "Some problems of cloud physics" in the memory of S.M. Shmeter, Russian Hydrometeorological Service, Central Aerological Observatory, Moscow, 478 p., ISBN: 5-7699-0023-3, ISSN: 0130-2906 "Meteorology and Hydrology".

Dixon, M. and Wiener, G., 1993: TITAN: Thunderstorm identification, tracking, analysis, and nowcasting—A radar-based methodology. Journal of atmospheric and oceanic technology, 10(6), pp.785-797.

Field, P. R., Wood, R., Brown, P. R. A., Kaye, P. H., Hirst, E., Greenaway, R., and Smith, J. A., 2003: Ice particle inter-arrival times measured with a Fast FSSP, J. Atmos. Ocean. Tech., 20, 249–261.

Gabriel, R.K. and Baras, M., 1970. The Israeli rainmaking experiment 1961-67: Final statistical tables and evaluation. Hebrew University.

Gagin, A., & Neumann, J. (1981). The second Israeli randomized cloud seeding experiment: Evaluation of the results. Journal of Applied Meteorology and Climatology, 20(11), 1301-1311.

Gayatri, K., and Coauthors, 2022: Evaluation of high-resolution WRF model forecasts and their use for cloud seeding decisions. J. Atmos. Solar-Terrestrial Phys., 228, 105825, https://doi.org/10.1016/j.jastp.2022.105825.

Geresdi, I., Xue, L., Chen, S., Wehbe, Y., Bruintjes, R., Lee, J.A., Rasmussen, R.M., Grabowski, W.W., Sarkadi, N. and Tessendorf, S.A., 2021. Impact of hygroscopic seeding on the initiation of precipitation formation: results of a hybrid bin microphysics parcel model. *Atmospheric Chemistry and Physics*, *21*(21), pp.16143-16159.

Guo, X., and G. Zheng, 2009: Advances in weather modification from 1997 to 2007 in China. Adv. Atmos. Sci., 26, 240–252, https://doi.org/10.1007/s00376-009-0240-8.

——, D. Fu, Z. Hu, 2013: Progress in cloud physics, precipitation, and weather modification during 2008–2012. Chinese Journal of Atmospheric Sciences, 37(2): 351-363 (in Chinese).

——, D. Fu, X. Li, Z. Hu, H. Lei, H. Xiao, and Y. Hong, 2015: Advances in cloud physics and weather modification in China. Adv. Atmos. Sci., 32, 230–249, https://doi.org/10.1007/s00376-014-0006-9.

Hosari, Al., T., and Coauthors, 2021: The UAE Cloud Seeding Program: A statistical and physical evaluation. Atmosphere (Basel)., 12, 1013, https://doi.org/10.3390/atmos12081013.

Jayachandran, V., and Coauthors, 2022a: Hygroscopic growth and CCN activation of aerosols during Indian Summer Monsoon over a rain-shadow region. Atmos. Res., 267, 105976, https://doi.org/10.1016/j.atmosres.2021.105976.

Jayachandran, V., P. D. Safai, P. S. Soyam, N. Malap, S. P. Bankar, M. Varghese, and T. V. Prabha, 2022b: Characterization of carbonaceous aerosols during the Indian summer monsoon over a rain-shadow region. Air Qual. Atmos. Heal., 15, 1713–1728, https://doi.org/10.1007/s11869-022-01211-1.

Jayachandran, V. N., and Coauthors, 2020: Cloud condensation nuclei characteristics during the Indian summer monsoon over a rain-shadow region. Atmos. Chem. Phys., 20, 7307–7334, https://doi.org/10.5194/acp-20-7307-2020.

Khelif, D., S. P. Burns, and C. A. Friehe, 1999: Improved wind measurements on research aircraft. J. Atmos. Ocean. Technol., 16, 860–875, https://doi.org/10.1175/1520-0426(1999)016<0860:IWMORA>2.0.CO;2.

Konwar, M., B. A. Raut, Y. J. Rao, and T. Prabhakaran, 2022: Rain microphysical properties over the rain shadow region of India. Atmos. Res., 275, 106224, https://doi.org/10.1016/j.atmosres.2022.106224.

Korolev, A. V., 2007: Reconstruction of the sizes of spherical particles from their shadow images. Part I: Theoretical considerations, J. Atmos. Ocean. Tech., 24, 376–389.

Korolev, A. and Field, P.R., 2015: Assessment of the performance of the inter-arrival time algorithm to identify ice shattering artifacts in cloud particle probe measurements. Atmospheric Measurement Techniques, 8(2), pp.761-777.

Koshida, T., M. Murakami, K. Yoshida, F. Fujibe, and K. Takahashi, 2012: Assessment of clouds suitable for summertime precipitation augmentation over Shikoku Island. SOLA, 8, 160–164, https://doi.org/10.2151/sola.2012-039.

Kuba, N., and M. Murakami, 2010: Effect of hygroscopic seeding on warm rain clouds – numerical study using a hybrid cloud microphysical model. Atmos. Chem. Phys., 10, 3335–3351, https://doi.org/10.5194/acp-10-3335-2010.

Lance, S., 2012: Coincidence errors in a Cloud Droplet Probe (CDP) and a Cloud and Aerosol Spectrometer (CAS), and the improved performance of a modified CDP. J. Atmos. Ocean. Technol., 29, 1532–1541, https://doi.org/10.1175/JTECH-D-11-00208.1.

Lance, S., C. A. Brock, D. Rogers, and J. A. Gordon, 2010: Water droplet calibration of the Cloud Droplet Probe (CDP) and in-flight performance in liquid, ice and mixed-phase clouds during ARCPAC. Atmos. Meas. Tech., 3, 1683–1706, https://doi.org/10.5194/amt-3-1683-2010.

Lin, K. I., Chung, K. S., Wang, S. H., Chen, L. H., Liou, Y. C., Lin, P. L., ... & Chang, Y. H. (2023). Evaluation of hygroscopic cloud seeding in warm rain process by a hybrid microphysics scheme on WRF model: a real case study. EGUsphere, 2023, 1-27.

Malap, N., T. V. Prabha, and A. Karipot, 2021: Impact of middle atmospheric humidity on boundary layer turbulence and clouds. J. Atmos. Solar-Terrestrial Phys., 215, 105553, https://doi.org/10.1016/j.jastp.2021.105553.

Manton, M. J., L. Warren, S. L. Kenyon, A. D. Peace, S. P. Bilish, and K. Kemsley, 2011: A Confirmatory Snowfall Enhancement Project in the Snowy Mountains of Australia. Part I: Project Design and Response Variables. J. Appl. Meteorol. Climatol., 50, 1432–1447, https://doi.org/10.1175/2011JAMC2659.1.

Martinez-Castro D, Pérez-Sanchez CA, Koloskov BP, Korneev VV, Petrov VV, Struinin M, Gamboa-Romero F, Novo-Cuervo S (2011) Randomized convective cloud seeding experiment in extended areas in Cuba (EXPAREX). Rev Bras Meteorol 26:515–528

Mather, G. K., D. E. Terblanche, F. E. Steffens, and L. Fletcher, 1997: Results of the South African cloud-seeding experiments using hygroscopic flares. J. Appl. Meteorol., 36, 1433–1447, https://doi.org/10.1175/1520-0450(1997)036<1433:ROTSAC>2.0.CO;2.

Murakami, M. and JCSEPA research group, 2011: Japanese Cloud Seeding Experiments for Precipitation Augmentation (JCSEPA) –New approaches and some results from wintertime and summertime weather modification programs. 10th WMO Scientific Conference on Weather Modification 2011, 2.

Murty, A. S. R., Coauthors, 2000: 11-year warm cloud seeding experiment in Maharashtra State, India. J Wea Mod, 32, 10–20

Nesterenko, P. N., 2001: Simultaneous separation and detection of anions and cations in ion chromatography. TrAC Trends Anal. Chem., 20, 311–319, https://doi.org/10.1016/S0165-9936(01)00072-3.

Orsini, D. A., Y. Ma, A. Sullivan, B. Sierau, K. Baumann, and R. J. Weber, 2003: Refinements to the particle-into-liquid sampler (PILS) for ground and airborne measurements of water soluble aerosol composition. Atmos. Environ., 37, 1243–1259, https://doi.org/10.1016/S1352-2310(02)01015-4.

Patil, C., N. Malap, A. Sathyanadh, B. Balaji, T. Prabhakaran, and A. Karipot, 2022: Moisture transport enhanced by the nocturnal low-level jet in association with the passage of a monsoon depression over the Indian subcontinent. Atmos. Res., 272, 106123, https://doi.org/10.1016/j.atmosres.2022.106123.

Raut, B. A., V. Louf, K. Gayatri, P. Murugavel, M. Konwar, and T. Prabhakaran, 2020: A multiresolution technique for the classification of precipitation echoes in radar data. IEEE Trans. Geosci. Remote Sens., 58, 5409–5415, https://doi.org/10.1109/TGRS.2020.2965649.

——, and Coauthors, 2021: Microphysical origin of raindrop size distributions during the Indian Monsoon. Geophys. Res. Lett., 48, https://doi.org/10.1029/2021GL093581.

Renggono, F., and Coauthors, 2022: Hygroscopic ground-based generator cloud seeding design; A case study from the 2020 weather modification in Larona Basin Indonesia. Atmosphere (Basel)., 13, 968, https://doi.org/10.3390/atmos13060968.

Resmi, E. A., and Coauthors, 2019: Observed diurnal and intraseasonal variations in boundary layer winds over Ganges valley. J. Atmos. Solar-Terrestrial Phys., 188, 11–25, https://doi.org/10.1016/j.jastp.2019.03.012.

Roberts, G. C., and A. Nenes, 2005: A continuous-flow streamwise thermal-gradient CCN chamber for atmospheric measurements. Aerosol Sci. Technol., 39, 206–221, https://doi.org/10.1080/027868290913988.

Rose, D., Gunthe, S.S., Mikhailov, E., Frank, G.P., Dusek, U., Andreae, M.O. and Pöschl, U., 2008: Calibration and measurement uncertainties of a continuous-flow cloud condensation nuclei counter (DMT-CCNC): CCN activation of ammonium sulfate and sodium chloride aerosol particles in theory and experiment. Atmospheric Chemistry and Physics, 8(5), pp.1153-1179.

Rosenfeld, D., Axisa, D., Woodley, W.L. and Lahav, R., 2010: A quest for effective hygroscopic cloud seeding. Journal of applied meteorology and climatology, 49(7), pp.1548-1562.

Rosenfeld, D. "The third Israeli randomized cloud seeding experiment in the south: Evaluation of the results and review of all three experiments." In Preprints, 14th Conf. on Planned and Inadvertent Weather Modification, Everett, WA, Amer. Meteor. Soc, pp. 565-568. 1998.

Safai, P. D., M. P. Raju, K. B. Budhavant, P. S. P. Rao, and P. C. S. Devara, 2013: Long term studies on characteristics of black carbon aerosols over a tropical urban station Pune, India. Atmos. Res., 132–133, 173–184, https://doi.org/10.1016/j.atmosres.2013.05.002.

Sakai, T., T. Nagai, N. Orikasa, Y. Zafizen, K. Yamashita, Y. Mano, and M. Murakami, 2013: Aerosol characterization by dual-wavelength polarization lidar measurements over Kochi, Japan during the warm seasons of 2008 to 2010. J. Meteorol. Soc. Japan. Ser. II, 91, 789–800, https://doi.org/10.2151/jmsj.2013-605.

Samanta, S., P. Murugavel, D. Gurnule, Y. J. Rao, J. Vivekanandan, and T. V. Prabha, 2021a: The life cycle of a stationary cloud cluster during the Indian Summer Monsoon: A microphysical investigation using polarimetric C-band radar. Mon. Weather Rev., 149, 3761–3780, https://doi.org/10.1175/MWR-D-20-0274.1.

——, T. V. Prabha, P. Murugavel, and P. Suneetha, 2021b: Rainfall types in the lifecycle of a stationary cloud cluster during the Indian Summer Monsoon: An investigation with numerical simulations and radar observation. Atmos. Res., 263, 105794, https://doi.org/10.1016/j.atmosres.2021.105794.

——, ——, ——, and ——, 2023: Morphological and microphysical characteristics associated with the lifecycle of a stationary cloud cluster during the Indian Summer Monsoon: A comparative study with numerical simulations and radar observation. Atmos. Res., 281, 106464, https://doi.org/10.1016/j.atmosres.2022.106464.

Segal, Y., Khain, A., Pinsky, M., & Rosenfeld, D. (2004). Effects of hygroscopic seeding on raindrop formation as seen from simulations using a 2000-bin spectral cloud parcel model. *Atmospheric Research, 71*(1-2), 3-34.

Semeniuk, T., Bruintjes, R., Salazar, V., Breed, D., Jensen, T., and Buseck, P. 2014: Individual aerosol particles in ambient and updraft conditions below convective cloud bases in the Oman mountain region, J. Geophys. Res.-Atmos., 119, 2511–2528.

Silverman, B. A., and W. Sukarnjanaset, 2000: Results of the Thailand warm-cloud hygroscopic particle seeding experiment. J. Appl. Meteorol., 39, 1160–1175, https://doi.org/10.1175/1520-0450(2000)039<1160:ROTTWC>2.0.CO;2.

Solanki, R., N. Malap, K. Gayatri, Y. J. Rao, and T. Prabhakaran, 2022: Characteristics of a pre-monsoon dryline atmospheric boundary layer over the rain shadow region: A case study. Front. Remote Sens., 3, https://doi.org/10.3389/frsen.2022.1028587.

Soyam, P. S., P. D. Safai, S. Mukherjee, K. Todekar, S. Bankar, D. Gurnule, N. Malap, and T. Prabhakaran, 2021: Black carbon aerosols over a semi-arid rain shadow location in Peninsular India: Temporal variability and sources. J. Earth Syst. Sci., 130, 95, https://doi.org/10.1007/s12040-021-01610-5.

Strapp, J. W., W. R. Leaitch, and P. S. K. Liu, 1992: Hydrated and dried aerosol-size-distribution measurements from the particle measuring systems FSSP-300 probe and the deiced PCASP-100X probe. J. Atmos. Ocean. Technol., 9, 548–555, https://doi.org/10.1175/1520-0426(1992)009<0548:HADASD>2.0.CO;2.

Tessendorf, S. A., and Coauthors, 2010: Overview of the Queensland cloud seeding research program. J. Wea. Modif., 42, 33–48

Tessendorf, S. A., Chen, S., Weeks, C., Bruintjes, R., Rasmussen, R. M., & Xue, L. (2021). The influence of hygroscopic flare seeding on drop size distribution over south-east Queensland. Journal of Geophysical Research: Atmospheres, 126(6), e2020JD033771

Thomas, L., N. Malap, W. W. Grabowski, K. Dani, and T. V. Prabha, 2018: Convective environment in pre-monsoon and monsoon conditions over the Indian subcontinent: The impact of surface forcing. Atmos. Chem. Phys., 18, 7473–7488, https://doi.org/10.5194/acp-18-7473-2018.

Tonttila, J., Korpinen, A., Kokkola, H., Romakkaniemi, S., Fortelius, C. and Korhonen, H., 2022. Interaction between hygroscopic seeding and mixed-phase microphysics in convective clouds. Journal of Applied Meteorology and Climatology, 61(10), pp.1533-1547.

Varghese, M., and Coauthors, 2020: New particle formation observed from a rain shadow region of the Western Ghats, India. Toxicol. Environ. Chem., 102, 305–333, https://doi.org/10.1080/02772248.2020.1789134.

——, and Coauthors, 2021: Cloud and aerosol characteristics during dry and wet days of south-west monsoon over the rain shadow region of Western Ghats, India. Meteorol. Atmos. Phys., 133, 1299–1316, https://doi.org/10.1007/s00703-021-00811-3.

Wang, F., Z. Li, Q. Jiang, G. Wang, S. Jia, J. Duan, and Y. Zhou, 2019a: Evaluation of hygroscopic cloud seeding in liquid-water clouds: A feasibility study. Atmos. Chem. Phys., 19, 14967–14977, https://doi.org/10.5194/acp-19-14967-2019.

Wang, W., Z. Yao, J. Guo, C. Tan, S. Jia, W. Zhao, P. Zhang, and L. Gao, 2019b: The wxtra-area effect in 71 cloud seeding operations during winters of 2008–14 over Jiangxi Province, East China. J. Meteorol. Res., 33, 528–539, https://doi.org/10.1007/s13351-019-8122-1.

WMO (2000) Report on the WMO International Workshop on Hygroscopic Seeding: Experimental results, physical processes, and research needs, WMP Rep 35, WMO/TD Rep 1006, WMO, 68 pp.

Yamashita, K., M. Murakami, A. Hashimoto, and T. Tajiri, 2011: CCN ability of Asian mineral dust particles and their effects on cloud droplet formation. J. Meteorol. Soc. Japan. Ser. II, 89, 581–587, https://doi.org/10.2151/jmsj.2011-512.

Yamashita K., M. Murakami, T. Tajiri, A. Saito, H. Ohtake and N. Orikasa, 2015: “Frontier of Weather Modification Research” (Edited by Murakami et al.), Meteorological Research Note published by Japan Meteorological Society, 231, 279-289 (in Japanese).

Zahraie, B., Poursepahy Samian, H., Nasseri, M., and Taheri, S. M., 2021: Statistical evaluation of cloud seeding operations in Central Plateau of Iran in the 2015 water year. Journal of the Earth and Space Physics, 47(1), Spring 2021, P. 12